RSC Advances

PAPER

View Article Online
View Journal | View Issue

Check for updates

Cite this: *RSC Adv.*, 2023, **13**, 11234

Magnetic clusters and ferromagnetic spin glass in the novel hexagonal perovskite 12R-$Ba_4SbMn_3O_{12}$†

Xiaohui Yan,[a] Junkun Wu,[a] Xiuyun Lei,*[a] Lunhua He,[bcd] Wenbin Guo,*[a] Xiaojun Kuang [ae] and Congling Yin *[a]

A 12-layer hexagonal perovskite $Ba_4SbMn_3O_{12}$ (space group: $R\bar{3}m$; a = 5.72733(3) Å, and c = 28.1770(3) Å) has been synthesized by high-temperature solid-state reactions and studied using powder X-ray and neutron diffraction and magnetization measurements. This 12R polytype structure contains one corner-sharing (Sb, Mn)O_6 octahedron and a trimer of face-sharing MnO_6 octahedra per formula unit. $Ba_4SbMn_3O_{12}$ displays a paramagnetic state of the Mn_3 magnetic cluster at 100–200 K, which partially disassociates into individual Mn ions at 250–300 K. The ferromagnetic interaction between these Mn_3 clusters is mainly mediated by Mn^{3+} at the M1 site, leading to dynamic ferromagnetic clusters below T_D = ~70 K and ferromagnetic spin freezing transition at T_g = ~11.5 K. The stability of Mn_3 magnetic clusters in the 12R polytypes is related to the intracluster Mn–Mn distance.

Received 29th January 2023
Accepted 26th March 2023

DOI: 10.1039/d3ra00607g

rsc.li/rsc-advances

Open Access Article. Published on 11 April 2023. Downloaded on 1/20/2026 9:39:59 AM.
This article is licensed under a Creative Commons Attribution-NonCommercial 3.0 Unported Licence.

1 Introduction

Manganese oxides have been the focus of materials research for many decades owing to their technological applications as heterogeneous catalysts,[1] Li-ion batteries,[2,3] SOFC electrode materials,[4] CMR materials,[5] and quantum materials.[6,7] This has motivated the investigation of the hexagonal perovskite $BaMnO_{3-\delta}$ system, which shows a diversity of crystal structures and magnetic properties.[8–12] A series of $BaMnO_{3-\delta}$ polytypes (2H → 15R → 8H → 6H → 10H → 4H) have been found as the oxygen vacancy concentration δ increases.[8,11] Further perovskite polytypes may be produced when Mn and Ba are replaced by other cations.

Many Mn-substituted $BaM_xMn_{1-x}O_3$ systems have been investigated, for instance, with M = Ca,[13] In,[14,15] Sn,[16,17] Sb,[18] Ti,[19] Fe,[20] Ru,[21] Ir,[22] Nb,[23] and rare earth Ln.[24–26] This led to the discovery of a series of M-cation ordered 12R perovskites $Ba_4M_{1+x}Mn_{3-x}O_{12}$ (M = Ti^{4+} and Sn^{4+}),[17,19] $Ba_4MMn_3O_{11.5}$ (M = In^{3+} and Y^{3+})[14,27] and $Ba_4MMn_3O_{12}$ (M = Nb^{5+}, Ce^{4+}, and Pr^{4+}).[23,26]

The 12R perovskite $Ba_4MMn_3O_{12}$ contains close-packed BaO_3 layers in a $(cchh)_3$ sequence and accommodates the M and Mn ions in the corner-sharing octahedral centre M1 and face-sharing octahedral centres M2 and M3 respectively (Fig. 1a). Partial disorder of M and Mn elements occurs on the M2 site in case of M = Ti^{4+} and Sn^{4+},[17,19] and oxygen vacancies are present for the M = In^{3+} and Y^{3+} case.[14,27]

Polymorphs of $BaMnO_{3-\delta}$ have long-range antiferromagnetic (AFM) order of all the Mn spins, with T_N = 220–270 K.[10,11] However, the long-range magnetic order is suppressed in the 12R perovskites upon low-level nonmagnetic doping, and the substituted M ions plays a key role in the magnetic behaviour of these materials. $Ba_4YMn_3O_{11.5}$,[27] $Ba_4Sn_{1.1}Mn_{2.9}O_{12}$ (ref. 17) and $Ba_4CeMn_3O_{12}$ (ref. 24) undergo an AFM transition at T_N = 4–6 K, while $Ba_4InMn_3O_{11.5}$ (ref. 14) and $Ba_4Ti_2Mn_2O_{12}$ (ref. 19) display

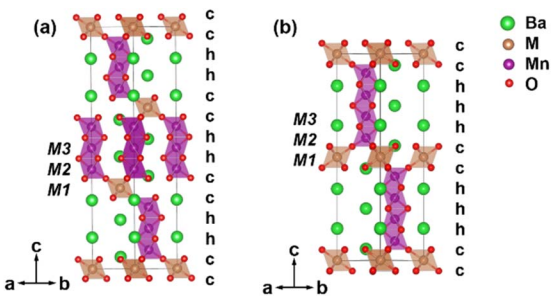

Fig. 1 The crystal structures of (a) 12R $Ba_4MMn_3O_{12}$ and (b) 10H $Ba_5MMn_4O_{15}$ viewed along [110], showing the stacking sequence of BaO_3 and corner-sharing octahedron center M1 and face-sharing octahedron center M2 and M3. Color code: barium (green sphere), M (orange sphere), manganese (purple sphere), oxygen (red sphere), MnO_6 (purple octahedron), and MO_6 (orange octahedron).

[a]*MOE Key Laboratory of New Processing Technology for Nonferrous Metal and Materials, Guangxi Key Laboratory of Optic and Electronic Materials and Devices, College of Materials Science and Engineering, Guilin University of Technology, Guilin 541004, P. R. China. E-mail: xylei@glut.edu.cn; guo0281@163.com; congling.yin@glut.edu.cn*

[b]*Spallat. Neutron Source Sci. Ctr, Dongguan 523803, P. R. China*

[c]*Chinese Acad Sci, Inst Phys, Beijing Natl Lab Condensed Matter Phys, Beijing 100190, P. R. China*

[d]*Songshan Lake Mat Lab, Dongguan 523808, P. R. China*

[e]*College of Chemistry and Bioengineering, Guilin University of Technology, Guilin 541004, P. R. China*

† Electronic supplementary information (ESI) available. CCDC 2212931. For ESI and crystallographic data in CIF or other electronic format see DOI: https://doi.org/10.1039/d3ra00607g

© 2023 The Author(s). Published by the Royal Society of Chemistry

Open Access Article. Published on 11 April 2023. Downloaded on 1/20/2026 9:39:59 AM.
This article is licensed under a Creative Commons Attribution-NonCommercial 3.0 Unported Licence.

no magnetic order, and $Ba_4NbMn_3O_{12}$ shows a ferrimagnetic transition at $T_C = 42$ K (ref. 23) (Table S1†). Furthermore, the Nb, Ti and Sn-doped 12R polytype show meta-magnetism, with linear Mn_3 magnetic clusters arranged in a triangular lattice, leading to magnetic frustrations.[17,23,28] Therefore, the 12R perovskite materials are potential quantum materials, such as quantum spin liquid and spin ice. The exploration of new 12R perovskite $BaM_xMn_{1-x}O_3$ is of great concern.

In the $BaSb_{1-x}Mn_xO_3$ system, two perovskite polymorphs 6H $Ba_3MnSb_2O_9$ (ref. 29) and 10H $Ba_5Sb_{1-x}Mn_{4+x}O_{15-\delta}$ have been identified. The $Ba_5Sb_{1-x}Mn_{4+x}O_{15-\delta}$ has close-packed BaO_3 layers in $(cchhh)_2$ sequences and features tetramers of face-sharing MnO_6 octahedra (Fig. 1b).[18] Regarding the close relationship between the 10H and 12R polymorphs, one wonders whether the 12R perovskites $BaSb_{1-x}Mn_xO_3$ can exit. If the 12R $BaSb_{1-x}Mn_xO_3$ is stabilized, it would be a good material with magnetic clusters and frustration. Motived by such ideas, we started a series of investigations on the $BaSb_{1-x}Mn_xO_3$ materials. Herein we report the synthesis, crystal structure, and magnetic properties of 12R $Ba_4SbMn_3O_{12}$ perovskite.

2 Experimental

2.1 Synthesis

The polycrystalline $Ba_4SbMn_3O_{12}$ was synthesized from $BaCO_3$ (99.5%, Aladdin), $MnCO_3$ (99.95%, Aladdin), and Sb_2O_3 (99.9%, Aladdin) reagents with solid-state reaction methods. These starting materials were thoroughly mixed with alcohol in an agate mortar and pestle and heated in a platinum crucible at 1173 K for 10 hours to decompose the carbonates. The materials were then reground, pressed into pellets (20 ton cm^{-2}), placed on platinum crucibles, and sintered at 1573 K for 36 hours with heating and cooling rates of 5 K min^{-1}. At several intermediate steps, the materials were re-ground and re-pressed, and powder X-ray diffraction (XRD) was performed at each step to follow the reaction to completion.

2.2 Characterization

The phase purity of the samples was characterized by XRD using a PANalytical X'Pert Pro powder diffractometer with Cu Kα radiation at 40 kV and 40 mA. High-quality XRD data were collected on the 2θ range 5–120° at room temperature (RT) for Rietveld analysis carried out using the Topas Academic software.[30] Bond valence sum (BVS) was calculated using standard parameters with Brown and Altermatt's method.[31] Low-temperature XRD data were collected in the 5–298 K range with an interval of 10 K, using a Rigaku SmartLab X-ray diffractometer with Cu Kα radiation at 45 kV and 200 mA.

Time of flight (TOF) neutron powder diffraction (NPD) data were collected from a 5 g powder sample of $Ba_4SbMn_3O_{12}$ using the General-Purpose Powder Diffractometer (GPPD) at the China Scattering Neutron Source (CSNS, Dongguan, China). Scanning electron microscopy (SEM) imaging and X-ray energy dispersive spectroscopy (EDS) elemental analysis were carried out using a GeminiSEM 300 (ZEISS, Germany) scanning electron microscope with an Ultim Max (Oxford, U.K.) EDS spectrometer.

Magnetic measurements were performed on Quantum Design's MPMS-3 Superconducting Quantum Interference Device (SQUID) magnetometer. Direct-current (dc) magnetic susceptibility was recorded in a magnetic field of 1000 Oe while heating the sample from 2 K to 300 K after zero-field cooling (ZFC) and field cooling (FC). Alternating-current (ac) magnetization was measured with an ac amplitude of $\mu_0 h_{ac} = 10$ Oe at frequencies of $3 \leq f \leq 250$ Hz in the temperature range 5–15 K. Isothermal field-dependent magnetization was performed at the applied field from −6 to 6 T and temperature of 2 K, 5 K, 15 K, 20 K, 30 K, 40 K, 50 K, 60 K and 100 K.

3 Results and discussions

3.1 Phase formation

The initial $Ba_4SbMn_3O_{12}$ samples consisted of mixed 12R perovskite phase and Mn-rich phases such as 8H $BaMnO_{3-\delta}$ (marked with asterisks), due to the loss of antimony oxides during the sintering process (melting point of Sb_2O_5 and Sb_2O_3 are ~655 K and ~928 K).[32] The Mn-rich phase was reduced through extra Sb doping. The 12R perovskite phase was isolated as a single phase at the nominal composition of $Ba_4Sb_{1.03}Mn_3O_{12}$, while beyond this Sb doping level other impurity reflections were observed, as marked as arrows in Fig. 2.

The chemical composition of the nominal $Ba_4Sb_{1.03}Mn_3O_{12}$ sample is most likely to be consistent with the stoichiometric perovskite of $Ba_4SbMn_3O_{12}$, which is reasonably supported by the Ba : Sb : Mn ratio of 4.00(20) : 1.01(4) : 2.73(12) from the EDS elemental analysis (Fig. 3) and the following Rietveld refinements.

3.2 Crystal structure

The light oxygen atoms are not well located with X-ray diffraction in the presence of heavy elements such as barium. Neutron diffraction (ND) is more sensitive to oxygen because the neutron

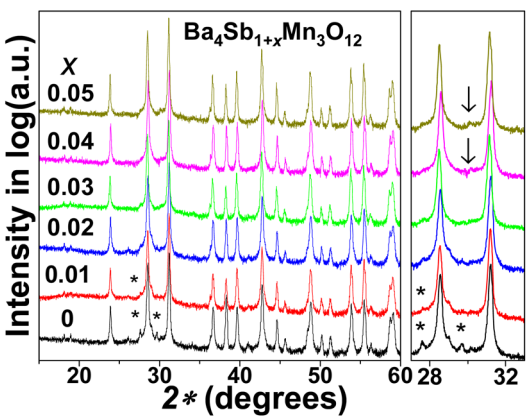

Fig. 2 XRD patterns of nominal $Ba_4Sb_{1+x}Mn_3O_{12}$ samples, showing a pure phase 12R perovskite at the $x = 0.03$ composition. The reflection from $BaMnO_{3-\delta}$ polymorphs and other impurities are marked with asterisks and arrows, respectively.

Open Access Article. Published on 11 April 2023. Downloaded on 1/20/2026 9:39:59 AM.
This article is licensed under a Creative Commons Attribution-NonCommercial 3.0 Unported Licence.

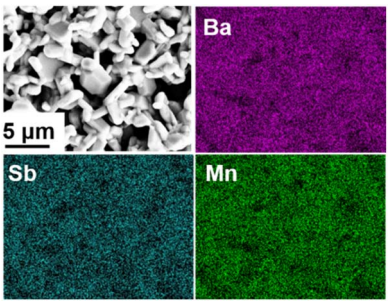

Fig. 3 SEM image and EDS elemental mapping image on the $Ba_4SbMn_3O_{12}$ sample, indicating the homogeneous distribution of elements.

scattering length of oxygen (5.083 fm) is comparable to that of Ba (5.07 fm).[33] Therefore, to find the accurate oxygen position, neutron diffraction data were collected on the $Ba_4SbMn_3O_{12}$ sample. The Rietveld refinements against the XRD and NPD data simultaneously were performed, based on the structural model of 12R $Ba_4NbMn_3O_{12}$ (Fig. 1a). During the refinements, the lattice parameters, the atomic coordinates, and the thermal displacement parameters (Beq) were varied freely. Anisotropic peak broadening was described with the Stephen model. In the first step, the occupancies of Sb and Mn at M1, M2, and M3 sites were refined with the total occupancies on each site subject to unity. A negative value of Sb on the M3 site was found, excluding the presence of Sb at the M3 site. In the following refinement, the occupancies of Sb and Mn were refined only at M1 and M2 sites, with the total ratio of Sb : Mn constrained as 1 : 3. In the second step, the oxygen occupancies were refined, and no vacancies were found at the oxygen sites within the refinement error. Therefore, the occupancies at both O1 and O2 sites were set as unity. The final refinement rapidly converged at the R_{wp} parameters of 5.50% and 4.32% for XRD and NPD data respectively (Fig. 4a and b). The refined structural parameters and selected bond distances and angles are summarized in Tables 1 and 2.

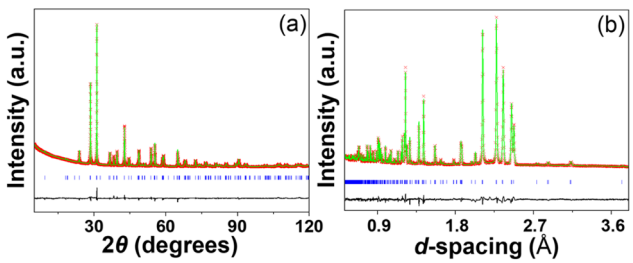

Fig. 4 Rietveld refinement plots of (a) XRD data and (b) ND data for the $Ba_4SbMn_3O_{12}$ sample, showing observed (red crosses), calculated (green line), and difference curve (grey line). The reflection positions for $Ba_4SbMn_3O_{12}$ are marked with blue bars in both plots.

In the crystal structure of 12R $Ba_4SbMn_3O_{12}$, Sb and Mn atoms are mixed on two crystallographic independent sites M1 and M2, with occupancy of 84% Sb/16% Mn and 8% Sb/92% Mn respectively. The BVS results listed in Table 1 show that the formal Mn charges are segregated, with Sb^{5+} and Mn^{3+} (which have similar ionic radii of 0.60 and 0.645 Å (ref. 34) respectively) at the corner-sharing M1 site, mixed Mn^{3+}, Mn^{4+} and Sb^{5+} at the M2 site, and Mn^{4+} at the M3 site. Based on the charge neutrality, this corresponds to the chemical formula $Ba_4(Sb1_{0.84}{}^{5+}Mn1_{0.16}{}^{3+})(Sb2_{0.08}{}^{5+}Mn2_{0.42}{}^{3+}Mn2_{0.5}{}^{4+})_2(Mn3^{4+})O_{12}$, where Mn1 corresponds to Mn at site M1, *etc.* This chemical formula has an average charge of Mn2 of +3.54, essentially identical to the BVS of 3.47.

The cationic distributions in $Ba_4SbMn_3O_{12}$ are different from those of the Sn, Y, and Nb-analogue.[17,23,27,35] In $Ba_4Sn_{1.1}Mn_{2.9}O_{12}$, Sn^{4+} and Mn^{4+} are mixed on the corner-sharing M1 (Sn : Mn ratio of 0.88 : 0.12) and face-sharing M2 (Sn : Mn ratio of 0.11 : 0.89) sites.[17] In $Ba_4YMn_3O_{11.5}$ and $Ba_4NbMn_3O_{12}$, the substituted Y^{3+}/Nb^{5+} and Mn^{4+}(and Mn^{3+}) ions are well separated over the M1 and M2 sites respectively. The structure of

Table 1 Refined structural parameters of $Ba_4SbMn_3O_{12}$[a]

Atom	Site	*x*, *y*, *z*	Occupancy	Beq	BVS
Ba1	6c	0, 0, 0.1288(1)	1	0.1(1)	2.22
Ba2	6c	0, 0, 0.2860(1)	1	0.7(2)	2.42
$(Sb/Mn)_{M1}$	3a	0, 0, 0	0.84/0.16(1)	1.9(1)	4.94/2.96
$(Mn/Sb)_{M2}$	6c	0, 0, 0.4110(1)	0.92/0.08(1)	0.5(1)	3.47/5.24
Mn_{M3}	3b	0, 0, 0.5	1	0.5(2)	3.89
O1	18h	0.4834(1), 0.5165(1), 0.1236(1)	1	0.7(1)	
O2	18h	0.4994(2), 0.5006(2), 0.2928(1)	1	1.1(2)	

[a] $a = 5.7273(1)$ Å, and $c = 28.1770(3)$ Å, space group: $R\bar{3}m$.

Table 2 Selected bond lengths and angles of $Ba_4SbMn_3O_{12}$

Bond length (Å)	Bond length (Å)	Bond angle (degree)
$(Sb/Mn)_{M1}$–O2 (×6) 2.014 (2)	Mn_{M3}–O1 (×6) 1.921 (1)	$(Sb/Mn)_{M1}$–O2–Mn_{M2} 177.97 (7)
$(Mn/Sb)_{M2}$–O1 (×3) 1.972 (2)	Mn_{M2}–Mn_{M3} 2.506 (2)	Mn_{M2}–O1–Mn_{M3} 80.14 (5)
$(Mn/Sb)_{M2}$–O2 (×3) 1.953 (2)		

© 2023 The Author(s). Published by the Royal Society of Chemistry

Open Access Article. Published on 11 April 2023. Downloaded on 1/20/2026 9:39:59 AM. This article is licensed under a Creative Commons Attribution-NonCommercial 3.0 Unported Licence.

$Ba_4SbMn_3O_{12}$ contains a higher proportion of magnetic Mn^{3+} cations (~16%) at the M1 sites that interconnect the Mn_3O_{12} trimers of face-sharing octahedra, which has a strong impact on the magnetic properties as discussed in the following sections.

It should be noted about the distortion of the outer MnO_6 octahedra in the trimers. The Mn_{M2} atom shifts toward the c-BaO_3 layers, forming three short Mn–O bonds (~1.95 Å) and three long ones (~1.97 Å), while the inner $Mn_{M3}O_6$ octahedron has no distortion constrained by its local site symmetry (D_{3d}). This leads to a short Mn–Mn distance d_{Mn-Mn} of ~2.5 Å inside the Mn_3O_{12} trimer, which is comparable with that in the elemental α-Mn.[36] This phenomenon could indicate a degree of d-orbital overlap between neighboring Mn ions forming Mn_3 magnetic clusters.

Phase stability of $Ba_4SbMn_3O_{12}$ was investigated by low-temperature XRD (Fig. 5a). No phase transition was observed in the range of 5–298 K. The lattice parameters and cell volume keep constant below ~70 K and increase linearly as temperature increases above 70 K, showing thermal expansion coefficient of $\alpha_a = 7.9 \times 10^{-6}$ K^{-1}, $\alpha_c = 7.0 \times 10^{-6}$ K^{-1} and $\alpha_V = 2.2 \times 10^{-5}$ K^{-1}.

3.3 Magnetic properties

The dc magnetization data for $Ba_4SbMn_3O_{12}$ (Fig. 6a) were corrected against two background terms: the susceptibility of the capsule determined as -5.6×10^{-6} emu with a blank measurement, and the diamagnetic susceptibility of $Ba_4SbMn_3O_{12}$, which can be estimated as -2.91×10^{-4} emu f.u.$^{-1}$ (or equally -1.00×10^{-4} emu per mol Mn^{4+}) using Pascal's constant.[37] The susceptibilities are nearly constant above 150 K and increase as the temperature goes down, which is typical for localized spin systems. A broad peak in magnetic susceptibilities (χ_{dc}) appears at around $T_m = 10.5$ K, indicating a magnetic phase transition. Ferromagnetic components are present below T_C as suggested by the divergent ZFC and FC susceptibilities.

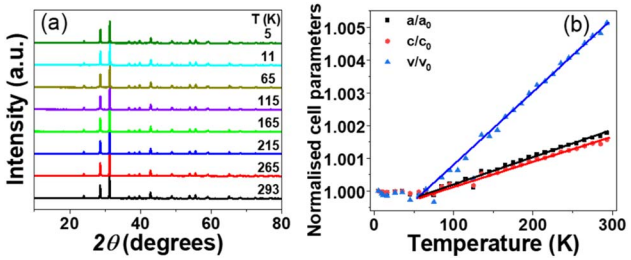

Fig. 5 Temperature-dependent (a) XRD data for $Ba_4SbMn_3O_{12}$ and (b) cell parameters relative to the 5 K values ($a_0 = 5.72318(9)$ Å, $c_0 = 28.1536(6)$ Å, $V_0 = 798.62(3)$ Å^3), with the fits shown as the solid lines.

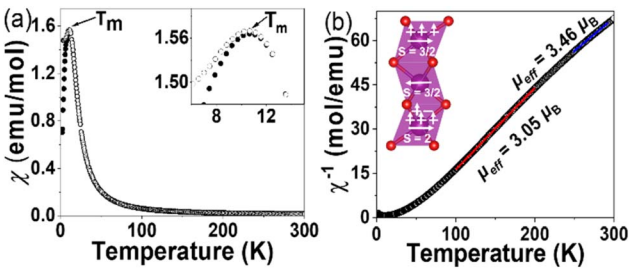

Fig. 6 (a) ZFC (filled circles) and FC (empty circles) magnetic susceptibility for $Ba_4SbMn_3O_{12}$ per mol Mn, with low-temperature data shown in the inset. (b) Inverse magnetic susceptibilities. The red and blue lines show the linear fits on 100–200 K and 250–300 K, corresponding to $\mu_{eff} = 3.05$ and $3.46\mu_B$ per mol Mn. The inset to (b) shows the schematics of the most possible arrangements of Mn^{3+} and Mn^{4+} in the Mn_3 magnetic clusters of $Ba_4SbMn_3O_{12}$.

The susceptibilities between 100 and 200 K can be well fitted based on the equation $\chi = C/(T - \theta)$, yielding the Weiss temperature θ_{cw} of ~43.4 K and $C \sim 1.16$ emu K mol^{-1} (Fig. 6b). This corresponds to a paramagnetic moment μ_{eff} of ~$3.05\mu_B$ per mol Mn or ~$5.28\mu_B$ per mol Mn_3 cluster. The former is significantly smaller than the expected value of $4.24\mu_B$ calculated from spin only Mn^{3+} : Mn^{4+} moment in the proportion 1 : 2, and this contradicts the paramagnetic states of individual Mn spins. The latter value is essentially identical to the expected values of ~$4.89\mu_B$, as estimated with the most possible Mn_3 cluster of $Ba_4SbMn_3O_{12}$ containing one terminal Mn^{3+} and two Mn^{4+} ions (Fig. 6b inset). This observation indicates the stabilization of Mn_3 magnetic clusters in a paramagnetic state at 100–200 K. Ferro- or ferri-magnetic interactions occur between the Mn_3 clusters as indicated by the positive $\theta_{cw} \sim 43.4$ K.

The Curie–Weiss fits of magnetic susceptibility at 250–300 K range leads to an $\mu_{eff} = 3.45(1)\mu_B$ per mol Mn or $\mu_{eff} = 5.98\mu_B$ per mol Mn_3 cluster equally. This result is larger than the expected value of Mn_3 clusters and smaller than that of Mn ions. This phenomenon indicates the Mn_3 magnetic cluster is partially destroyed, leading to the coexistence of individual Mn ions and Mn_3 clusters in this temperature range, although an exclusively paramagnetic state of Mn ions requires a higher temperature.

Similar Mn_3 magnetic clusters have been evidenced with different stability in 12R Sn- and Nb-doped analogs.[17,23] Compared with that in $Ba_4SbMn_3O_{12}$ ($d_{Mn-Mn} = \sim 2.506$ Å), the Mn_3 cluster in $Ba_4NbMn_3O_{12}$ ($d_{Mn-Mn} = \sim 2.469$ Å) is more stable without dissociation at RT,[23] while the Mn_3 cluster in $Ba_4Sn_{1.1}Mn_{2.9}O_{12}$ ($d_{Mn-Mn} = \sim 2.523$ Å) is unstable at RT and split into Mn ions.[17] The stability of Mn_3 clusters can be associated with the intra-cluster d_{Mn-Mn}. A smaller Mn–Mn distance would mediate stronger direct exchange interactions *via* a greater overlap between the t_{2g} orbitals of Mn ions, leading to greater stability of Mn_3 clusters in these 12R perovskites.

Isothermal *M–H* data were performed at 2–100 K to study the magnetic ground states of $Ba_4SbMn_3O_{12}$ (Fig. 7a). Linear *M–H* dependence at 100 K is consistent with the paramagnetic states of Mn_3 clusters. Magnetic hysteresis and saturation are observed at 2–60 K. In contrast with the isotropic magnetization at 15–60 K, small magnetic anisotropy is observed with a coercive field of 100 mT and 12 mT at 2 K and 5 K respectively. This indicates $Ba_4SbMn_3O_{12}$ displays a ferro- or ferri-magnetic state below 60 K. The saturated moment M_s can be estimated with the intercept from the linear *M–H* fit at the high field range. Being a constant of ~$1.61\mu_B$ at 2–5 K, the M_s decreases linearly at increasing temperatures above T_C and disappears at $T_D \sim 70$ K from extrapolation (Fig. 7b). Here, T_D represents the

Open Access Article. Published on 11 April 2023. Downloaded on 1/20/2026 9:39:59 AM.
This article is licensed under a Creative Commons Attribution-NonCommercial 3.0 Unported Licence.

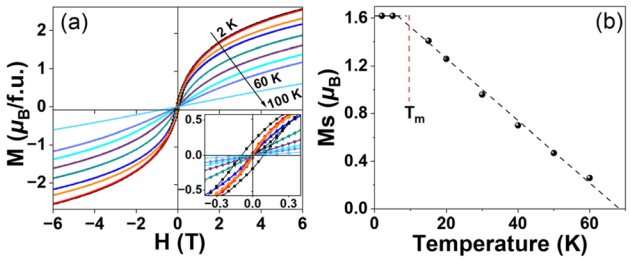

Fig. 7 (a) Magnetization of $Ba_4SbMn_3O_{12}$ from −6 T to 6 T at various temperatures. The inset expands the M–H curves at the low-field region. (b) The saturated moment M_S, with the variation trends shown in dashed lines.

temperature dynamical ferromagnetic clusters initially form, while T_C represents the spin-freezing temperature. This critical linear behavior is different from the saturation behavior in typical long-range ferromagnet $SrFe_{0.5}Co_{0.5}O_3$,[38] and indicates the nature of ferromagnetic spin glass.[39] The T_D/T_C of about 6 keeps with those observed in other spin glass systems.[40,41]

The spin-glass behavior is further studied by the ac susceptibility, and the real (and imaginary) component of the ac susceptibility χ' (and χ'') *versus* temperature at different frequencies is plotted in Fig. 8 (and Fig. S1†). The peak in dc susceptibility at $T_m \approx 10.5$ K appears to be a frequency-dependent peak in the ac susceptibilities. The temperature T_m at the broad peak maximum shifts to higher values as the frequency increases (Fig. 8 bottom inset). The frequency dependence of T_m can be well fitted to a critical power law (Fig. 8 top inset),[41,42] with the best power-law fit,

$$\tau = \tau_0 \left(\frac{T_m}{T_g} - 1 \right)^{-zv}$$

where $\tau = (2\pi f)^{-1}$, τ_0 is the average relation time and T_g is the static glassy transition temperature, and zv is the dynamic

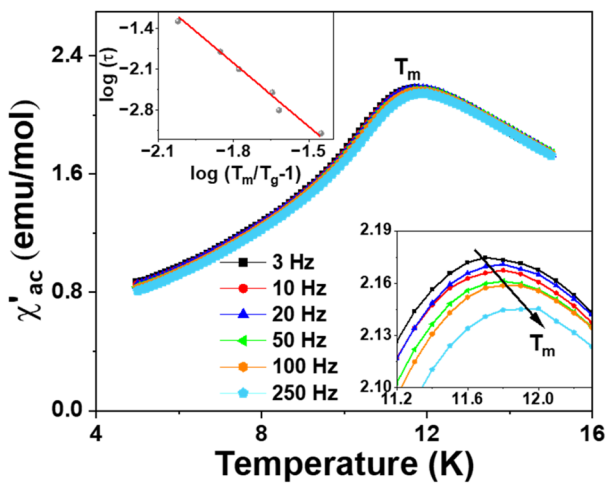

Fig. 8 Temperature dependence of the real ac susceptibility component χ' at frequencies of $3 \leq f \leq 250$ Hz. The bottom inset shows the data around T_m for clarity. The top inset shows the frequency dependence of the freezing temperature T_m with the best power-law fit.

critical exponent. The fitted $T_g = 11.6(3)$ K is close to the T_m in dc susceptibilities. The $\tau_0 = 10^{-8.3(6)}$ s keeps with the fitted characteristic relation time of 10^{-8} to 10^{-12} s for canonical spin glass,[41–43] while the $zv = 3.5(7)$ is also comparable to that in typical spin glass materials.

Another important factor for characterizing a magnetic glassy transition is the frequency shift K, which gives a relative variation in the peak temperature T_m with the angular frequency and is defined as follows:

$$K = \frac{1}{T_m} \frac{\Delta T_m}{\Delta \log \omega}$$

The frequency shift K on $Ba_4SbMn_3O_{12}$ is estimated to be about 0.016, much smaller than the values for super-paramagnets and close to those observed in spin glasses. This indicates the magnetic state of $Ba_4SbMn_3O_{12}$ is a spin glass rather than a super-paramagnet.

The magnetic saturation and frustration blew T_C may arise from the partial occupancy of Mn^{3+} at the M1 sites, as observed in $Ba_5Sb_{1-x}Mn_{4+x}O_{15-\delta}$ systems.[18] The dominant magnetic super-exchange interactions between Mn_3 magnetic clusters are associated with the near-linear M1–O–M2 connections in the 12R structure type (see Table 2). The hexagonal average lattice symmetry is incompatible with long-range orbital order, but when Mn^{3+} ions are present at the M1 sites, local orbital order concerning the Mn^{3+} and Mn^{4+} ions at the six neighboring M2 sites is likely in such a highly connected manganite network. This gives rise to a mixture of strong ferromagnetic $Mn_{M1}{}^{3+}$–O–$Mn_{M2}{}^{4+}$ and antiferromagnetic $Mn_{M1}{}^{3+}$–O–$Mn_{M2}{}^{3+}$ interactions (both types are found in long-range orbitally ordered and spin-ordered manganites such as $La_{0.5}Ca_{0.5}MnO_3$ and $LaMnO_3$ (ref. 44)).

According to the $Sb_{M1}{}^{5+}$: $Mn_{M1}{}^{3+}$ ratio of ~5.25, we can assume each Mn_3 trimer connects with six Sb^{5+} or five Sb^{5+} and one Mn^{3+} on the adjacent M1 site, while each $Mn_{M1}{}^{3+}$ has six Mn_3 trimers as neighbors. As a result, about 96% of Mn_3 clusters assemble into isolated superclusters of $(Mn_3)_6Mn^{3+}$ *via* Mn^{3+} on the M1 site, while minor (~4%) Mn_3 clusters are isolated with six adjacent Sb^{5+} ions. The local $(Mn_3)_6Mn^{3+}$ supercluster possesses three kinds of Mn_{M2}–O–$Mn_{M1}{}^{3+}$–O–Mn_{M2} linear bridge related to the charge state of terminal Mn ions. The charge symmetric bridges $Mn_{M2}{}^{4+}$–O–$Mn_{M1}{}^{3+}$–O–$Mn_{M2}{}^{4+}$ and $Mn_{M2}{}^{3+}$–O–$Mn_{M1}{}^{3+}$–O–$Mn_{M2}{}^{3+}$ would mediate a parallel alignment between Mn_3 clusters spins, while the charge asymmetric bridge $Mn_{M2}{}^{3+}$–O–$Mn_{M1}{}^{3+}$–O–$Mn_{M2}{}^{4+}$ would lead to an antiparallel alignment. As Sb^{5+}, Mn^{3+}, and Mn^{4+} mixes on the M2 site at the ratio of 0.08 : 0.42 : 0.5 (see Table 1), the Mn_{M2}–O–$Mn_{M1}{}^{3+}$–O–Mn_{M2} bridges in the $(Mn_3)_6Mn^{3+}$ supercluster consist of 42.64% charge-symmetric, 42% charge-asymmetric, and 15.36% diamagnetic Sb^{5+} ions containing ones. Therefore, these charge-symmetric Mn_{M2}–O–$Mn_{M1}{}^{3+}$–O–Mn_{M2} bridges would mediate 40.9% of all Mn_3 cluster spins frozen in a parallel arrangement in the magnetic ground state of 12R $Ba_4SbMn_3O_{12}$, and leads to expected saturated moments of $1.63\mu_B$, which is essentially identical with the observed M_s of $1.61\mu_B$ at 2–5 K.

© 2023 The Author(s). Published by the Royal Society of Chemistry

Open Access Article. Published on 11 April 2023. Downloaded on 1/20/2026 9:39:59 AM.
This article is licensed under a Creative Commons Attribution-NonCommercial 3.0 Unported Licence.

The presence of a significant proportion of Mn^{3+} at the M1 sites in $Ba_4SbMn_3O_{12}$ appears to be essential for the pronounced ferromagnetism. This can be indicated by $Ba_4Sn_{1.1}Mn_{2.9}O_{12}$, which hosts Mn^{4+} and Sn^{4+} on the M1 site and displays weak ferromagnetism with M_s of $\sim 0.09\mu_B$ at 2 K. Compared with the magnetic Mn_4 cluster with all spin canceled, the Mn_3 cluster has net spins and also contributes to ferromagnetism. This explains the reduced ferromagnetism of 10H $Ba_5Sb_{1-x}Mn_{4+x}O_{15}$ with higher content of Mn^{3+} ($\sim$24–36%) on the M1 site compared with that of 12R $Ba_4SbMn_3O_{12}$. Further studies of magnetic order using theoretical calculation will be needed to account more fully for the spin ordering phenomena.

4 Conclusions

The new 12R perovskite $Ba_4SbMn_3O_{12}$ has been synthesized by high-temperature solid-state reactions. The material has an ordered arrangement of Sb and Mn cations, and trimers of face-sharing MnO_6 octahedra. The paramagnetic state of $Ba_4SbMn_3O_{12}$ at 100–200 K can be described with the Mn_3 magnetic clusters, which partially disassociate into individual Mn ions at 250–300 K. The stability of Mn_3 magnetic clusters in the 12R polytypes is related to the intracluster Mn–Mn distance. The ferromagnetic interaction between these Mn_3 clusters is mainly mediated by Mn^{3+} at the M1 site, leading to dynamic ferromagnetic clusters below $T_D = \sim 70$ K and ferromagnetic spin freezing transition at $T_g = \sim 11.5$ K. $Ba_4SbMn_3O_{12}$ is another rare example of a periodical lattice that shows cluster magnetism due to the cationic order beyond orbital molecules.[45]

Conflicts of interest

There are no conflicts to declare.

Acknowledgements

The National Natural Science Foundation of China (No. 51662013, 22161014, 21850410458), Guangxi Natural Science Foundation (No. 2020GXNSFAA297220, 2019GXNSFGA245006, AD19245097), and the Foundation of Guilin University of Technology (No. GUTQDJJ2018115) are acknowledged for their financial support.

Notes and references

1 Q. Feng, H. Kanoh and K. Ooi, *J. Mater. Chem.*, 1999, **9**, 319–333.
2 P. Strobel and C. Mouget, *Mater. Res. Bull.*, 1993, **28**, 93–100.
3 A. R. Armstrong and P. G. Bruce, *Nature*, 1996, **381**, 499–500.
4 M. Mogensen, K. V. Jensen, M. J. Jorgensen and S. Primdahl, *Solid State Ionics*, 2002, **150**, 123–129.
5 Y. Tokura, *Rep. Prog. Phys.*, 2006, **69**, 797–851.
6 A. J. Browne, A. Krajewska and A. S. Gibbs, *J. Mater. Chem. C*, 2021, **9**, 11640–11654.
7 L. T. Nguyen and R. Cava, *Chem. Rev.*, 2020, **121**, 2935–2965.
8 T. Negas and R. S. Roth, *J. Solid State Chem.*, 1971, **3**, 323–339.
9 E. J. Cussen and P. D. Battle, *Chem. Mater.*, 2000, **12**, 831–838.
10 J. J. Adkin and M. A. Hayward, *J. Solid State Chem.*, 2006, **179**, 70–76.
11 J. J. Adkin and M. A. Hayward, *Chem. Mater.*, 2007, **19**, 755–762.
12 J. Varignon and P. Ghosez, *Phys. Rev. B: Condens. Matter Mater. Phys.*, 2013, **87**, 140403.
13 N. Floros, C. Michel, M. Hervieu and B. Raveau, *Chem. Mater.*, 2000, **12**, 3197–3201.
14 N. Créon, C. Michel, M. Hervieu, A. Maignan and B. Raveau, *Solid State Sci.*, 2003, **5**, 243–248.
15 C. L. Yin, G. B. Li, T. N. Jin, L. P. You, J. Tao, J. W. Richardson, C. K. Loong, J. L. Sun, F. H. Liao and J. H. Lin, *Chem. Mater.*, 2008, **20**, 2110–2116.
16 C. L. Yin, G. B. Li, T. N. Jin, J. Tao, J. W. Richardson, C. K. Loong, F. H. Liao and J. H. Lin, *J. Alloys Compd.*, 2010, **489**, 152–156.
17 J. Wu, X. Yan, W. Guo, X. Wang, C. Yin and X. Kuang, *RSC Adv.*, 2021, **11**, 40235.
18 C. Yin, G. Li, W. A. Kockelmann, F. Liao, J. P. Attfield and J. Lin, *Chem. Mater.*, 2010, **22**, 3269–3276.
19 G. M. Keith, C. A. Kirk, K. Sarma, N. M. Alford, E. J. Cussen, M. J. Rosseinsky and D. C. Sinclair, *Chem. Mater.*, 2004, **16**, 2007–2015.
20 L. Miranda, D. C. Sinclair, M. Hernando, A. Varela, A. Wattiaux, K. Boulahya, J. M. Gonzalez-Calbet and M. Parras, *Chem. Mater.*, 2009, **21**, 5272–5283.
21 C. L. Yin, G. B. Li, W. A. Kockelmann, J. H. Lin and J. P. Attfield, *Phys. Rev. B: Condens. Matter Mater. Phys.*, 2009, **80**, 094420.
22 N. A. Jordan and P. D. Battle, *J. Mater. Chem.*, 2003, **13**, 2220–2226.
23 L. T. Nguyen, T. Kong and R. J. Cava, *Mater. Res. Express*, 2019, **6**, 056108.
24 M. A. Macias, O. Mentre, C. Pirovano, P. Roussel, S. Colis and G. H. Gauthier, *New J. Chem.*, 2015, **39**, 829–835.
25 C. L. Yin, G. F. Tian, G. B. Li, F. H. Liao and J. H. Lin, *RSC Adv.*, 2017, **7**, 33869.
26 A. F. Fuentes, K. Boulahya and U. Amador, *J. Solid State Chem.*, 2004, **177**, 714–720.
27 X. J. Kuang, C. Bridges, M. Allix, J. B. Claridge, H. Hughes and M. J. Rosseinsky, *Chem. Mater.*, 2006, **18**, 5130–5136.
28 S. V. Streltsov and D. I. Khomskii, *JETP Lett.*, 2018, **108**, 686–690.
29 Y. S. Doi, Y. Hinatsu and K. Ohoyama, *J. Phys.: Condens. Matter*, 2004, **16**, 8923–8935.
30 A. Coelho, *Coelho Software*, 2012.
31 I. D. Brown and D. Altermatt, *Acta Crystallogr.*, 1985, **41B**, 244–247.
32 P. Patnaik, *Handbook of Inorganic Chemicals*, McGraw-Hill Companies, Inc., New York, 2002.
33 V. F. Sears, *J. Neutron Res.*, 1992, **3**, 26–37.
34 R. D. Shannon, *Acta Crystallogr.*, 1976, **32A**, 751–767.
35 X. J. Kuang, H. Zhu, M. Allix, C. A. Bridges, M. J. Rosseinsky and Y. X. Li, *J. Mater. Chem.*, 2012, **22**, 8103–8109.

© 2023 The Author(s). Published by the Royal Society of Chemistry

Open Access Article. Published on 11 April 2023. Downloaded on 1/20/2026 9:39:59 AM.
This article is licensed under a Creative Commons Attribution-NonCommercial 3.0 Unported Licence.

36 J. A. Oberteuffer and J. A. Ibers, *Acta Crystallogr.*, 1970, **26B**, 1499–1504.
37 G. A. Bain and J. F. Berry, *J. Chem. Educ.*, 2008, **85**, 532–536.
38 C. Yin, Q. Liu, R. Decourt, M. Pollet, E. Gaudin and O. Toulemonde, *J. Solid State Chem.*, 2011, **184**, 3228–3231.
39 J. Crangle, *Solid State Magnetism*, Edward Arnold, 1991.
40 K. Binder and A. P. Young, *Rev. Mod. Phys.*, 1986, **86**, 801–963.
41 J. A. Mydosh, *Spin Glasses: An Experimental Introduction*, Taylor & Francis, London, 1993.
42 S. Bedanta and W. Kleemann, *J. Phys. D: Appl. Phys.*, 2009, **42**, 013001.
43 P. C. Hohenberg and B. I. Halperin, *Rev. Mod. Phys.*, 1977, **49**, 435–479.
44 E. Dagotto, T. Hotta and A. Moreo, *Phys. Rep.*, 2001, **344**, 1–153.
45 J. P. Attfield, *APL Mater.*, 2015, **3**, 041510.

© 2023 The Author(s). Published by the Royal Society of Chemistry